

# RRL Solar

Rapid Research Letters  
Full Papers · Reviews

**Acetamidinium Cation to Confer Ion Immobilization and Structure Stabilization of Organometal Halide Perovskite Toward Long Life and High-Efficiency p-i-n Planar Solar Cell via Air-Processable Method**

Kai-Chi Hsiao, Meng-Huan Jao, Kuo-Yu Tian, Ting-Han Lin, Dinh-Phuc Tran, Hsueh-Chung Liao, Cheng-Hung Hou, Jing-Jong Shyue, Ming-Chung Wu, and Wei-Fang Su

WILEY-VCH

# Acetamidinium Cation to Confer Ion Immobilization and Structure Stabilization of Organometal Halide Perovskite Toward Long Life and High-Efficiency p-i-n Planar Solar Cell via Air-Processable Method

Kai-Chi Hsiao, Meng-Huan Jao, Kuo-Yu Tian, Ting-Han Lin, Dinh-Phuc Tran, Hsueh-Chung Liao, Cheng-Hung Hou, Jing-Jong Shyue, Ming-Chung Wu, and Wei-Fang Su\*

Ion migration in organometal halide perovskite solar cell (OHPSC) and crystal structure evolution of organometal halide perovskites (OHPVSKs) in air are considered as one of the critical factors for unstable performance and of the urgent issues for the reliability of OHPSCs. Herein, a novel cation of acetamidinium ( $\text{Aa}^+$ ) with stronger coordinated bond with  $\text{I}^-$  than methylammonium is induced into OHPVSK to stabilize its crystal structure. By incorporating  $\text{Aa}^+$  ions into OHPVSKs, the power conversion efficiency (PCE) of OHPSC without an encapsulation can maintain higher than 75% of its initial PCE after a 200 h humidity (60–80% relative humidity (RH) in air) or a 24 h thermal stress test (85 °C in dry  $\text{N}_2$ ). The  $\text{Aa-MAPbI}_3$  device exhibits an outstanding efficiency of 20.68%, and over 80% of initial PCE is maintained after a 1300 h damp heat as encapsulated. This novel cation can be easily incorporated into OHPVSK via a hot casting process in air with a high environmental tolerance as compared with that from the conventional coating process, which suffers from sophisticated crystallization steps and a strict processing atmosphere. It extends processing windows for OHPVSK fabrication and provides a promising path toward mass production and further commercialization.

## 1. Introduction

The organometal halide perovskite solar cell (OHPSC) holds many advantages over other types of solar cells, such as high absorption coefficient in visible light,<sup>[1]</sup> low binding energy of its excitons,<sup>[2]</sup> long diffusion length of carriers,<sup>[3,4]</sup> tunable bandgap from various composition,<sup>[5–7]</sup> and solution processing. Researchers are continuously working to improve the power conversion efficiency (PCE) of OHPSCs since it first debuted in 2009.<sup>[8]</sup> The PCE of OHPSCs soars from 3.9%<sup>[8]</sup> to over 25%,<sup>[9]</sup> which is the best performance in thin-film photovoltaics. However, as sensitive materials to a surrounding environment, the durability of such devices is one of the main concerns for commercialization and industrialization of OHPSCs, which requires special attention.

In general, moisture and oxygen molecules in a surrounding environment are considered as major suspects to initiate the degradations of OHPSCs.<sup>[10,11]</sup> Therefore, a sophisticated environmental

K.-C. Hsiao, Dr. M.-H. Jao, K.-Y. Tian, Dr. D.-P. Tran, Dr. C.-H. Hou, Prof. J.-J. Shyue, Prof. W.-F. Su  
Department of Materials Science and Engineering  
National Taiwan University  
Taipei City 10617, Taiwan  
E-mail: suwf@ntu.edu.tw

K.-C. Hsiao, Prof. W.-F. Su  
Advanced Research Center for Green Materials Science and Technology  
National Taiwan University  
Taipei City 10617, Taiwan

T.-H. Lin  
Department of Chemical and Materials Engineering  
Chang Gung University  
Taoyuan City 33302, Taiwan

 The ORCID identification number(s) for the author(s) of this article can be found under <https://doi.org/10.1002/solr.202000197>.

Dr. H.-C. Liao  
FrontMaterials Corporation Ltd.  
Taipei City 10087, Taiwan

Dr. C.-H. Hou, Prof. J.-J. Shyue  
Research Center for Applied Sciences  
Academia Sinica  
Taipei City 11529, Taiwan

Prof. M.-C. Wu  
Green Technology Research Center  
Chang Gung University  
Taoyuan City 33302, Taiwan

Prof. M.-C. Wu  
Division of Neonatology  
Department of Pediatrics  
Chang Gung Memorial Hospital  
Taoyuan City 33305, Taiwan

DOI: 10.1002/solr.202000197

control for OHPSCs fabrication is commonly applied to prevent the OHPSC from the exposure of moisture and oxygen. The anionic and cationic defects in crystallized perovskite films, which are present at grain boundaries, are the primary pathways for moisture and oxygen diffusion. These gas molecules diffuse through these pathways and react with perovskite films, leading to PCE degradation of devices.<sup>[12–14]</sup> The defects may induce deep-level and/or shallow-level trap states accordingly to their type.<sup>[15–17]</sup> The defects originated from iodine and lead vacancies cause deep-level trap states and act as nonradiative recombination sites to generate defect-assisted photoluminescence (PL) decay.<sup>[18]</sup> It causes a dramatic impairment of the photovoltaic performance by the unexpected  $V_{oc}$  deficit of OHPSC.<sup>[19]</sup> For the shallow-level traps, although they have a minor adverse effect on PCE compared with deep-level trap state, their ionic nature creates an opportunity to become mobile ions and to migrate at the presence of electric field.<sup>[20–22]</sup> The accumulation of charge ions causes the band bending and let OHPSC suffer from unstable output during continuous operation.<sup>[23,24]</sup>

Therefore, the concepts of defect passivation have been explored to solve the issue of the deficit of PCE or the unstable output, and thus enhance the lifetime of OHPSCs.<sup>[19,25–29]</sup> Among the passivation strategies, dipolar ion molecules such as D-4-*tert*-butylphenylalanine, thiophene ethyl ammonium chloride (TEACL), and phenyl ethyl ammonium iodide are the ones which can simultaneously compensate both positive and negative ionic defects.<sup>[30–32]</sup> Despite the fact that defect passivation greatly enhances the PCE and stability of OHPSC, its effect is attributed to an external improvement in reducing the defect density at grain boundaries or the surface of perovskite films. The ion migration of methyl ammonium ( $MA^+$ ) and iodide ( $I^-$ ) ions in the perovskite film is still difficult to be completely eliminated by this kind of passivation. Even with a small number of defects in perovskite films, the ion migration occur because of their low activation energies and high diffusion coefficient.<sup>[33]</sup> Therefore, by inducing a molecule that can increase the amount of coordinated bonds with the  $I^-$  ions of perovskite lattice is another feasible method to not only immobilize the ions in lattice but also increase the stability of perovskite crystal structure under environmental stresses.<sup>[34]</sup>

An easy and straightforward method of hot casting is demonstrated in this study to overcome the aforementioned obstacles of strict environment and dedicated crystallization steps of perovskite film deposition. The uniqueness of hot casting method comes from the ultrafast step of perovskite crystallization that allows perovskite films to get rid of the restrict atmosphere ( $N_2$ -filled glove box) and to tolerate the presence of moisture (<10% RH) and oxygen molecules (in air) during perovskite deposition. In general, the cations of  $MA^+$ , formamminium ( $FA^+$ ), and cesium ( $Cs^+$ ) are used as the A-site cations to prepare perovskite crystal. Their appropriate ionic sizes allow them to construct a perovskite crystal structure. Although  $FA^+$  and  $Cs^+$  based perovskite are difficult to maintain the photoactive phase at room temperature, incorporating cation with different ionic sizes is an effective method to balance the Goldschmidt tolerance factor and to stabilize the  $FA^+$  and  $Cs^+$  based perovskite crystal structure.<sup>[35]</sup> A large A-site cation in perovskite is believed to enhance the thermal stability of perovskite crystal structure due to its size effect and high boiling point.<sup>[36,37]</sup>

Incorporation of a small amount ( $\approx 5$  mol%) of large size cation will induce minute lattice distortion, thus increasing the activation of ion migration. The undesirable ion migration will be retarded.<sup>[38]</sup> Furthermore, the large size cation will increase the coordination with  $I^-$ , thus stabilizing the crystal.<sup>[39]</sup> Therefore, a novel cation, acetaminiium ion ( $Aa^+$  cation), with a bigger ion radius, higher boiling point, and a larger amount of coordinated bonds with  $I^-$  ions than that of conventional  $MA^+$ , is induced into methyl ammonium lead triiodide perovskite ( $MAPbI_3$ ) to stabilize crystal structure and retard the ion migration.<sup>[40,41]</sup>

In this research, the improvement of cell performance and retard mechanism of ion migration using the film of  $Aa^+$  ion incorporated in  $MAPbI_3$  ( $Aa$ - $MAPbI_3$ ) were systematically studied using time-of-flight secondary ion spectrum (ToF-SIMS), X-ray diffraction (XRD), time-resolved photoluminescence spectrum (TR-PL), and space charge limit current (SCLC) modeling. After inducing 5 mol% of  $Aa^+$  ion into  $MAPbI_3$ ,  $Aa$ - $MAPbI_3$  device exhibits a higher environmental stress tolerance than the pristine  $MAPbI_3$  one. The efficiency of hot casted p-i-n planar solar cells using  $Aa$ - $MAPbI_3$  film can be enhanced from 18.60% to 20.68% and stable outputs can be achieved during 300 s continuous operation in air. The crystal structure of  $Aa$ - $MAPbI_3$  shows no deterioration after 200 h under humidity stress (30–38 °C and 60–80% RH in air) as well as 24 h under thermal stress (85 °C in dry  $N_2$ ). The  $Aa$ - $MAPbI_3$  devices could maintain over 80% of its initial PCE under the testing conditions without encapsulation and pass 1300 h damp heat tests (85 °C and 85% RH) as encapsulated. The results of ToF-SIMS, spectroscopy, electronic, and device characterizations revealed that  $Aa^+$  ions incorporated into  $MAPbI_3$  can hinder the ion migration triggering from environmental stresses and greatly improve the stability of such OHPSC.

## 2. Results and Discussion

The chemical structures of  $MA^+$  and  $Aa^+$  cations are shown in **Figure 1a**.  $MA^+$  ion is the most common A-site cation for OHPVSK. Note that  $Aa^+$  ion (radius = 2.77 Å) is larger cations and have more amine groups than those of  $MA^+$  ion (radius = 2.16 Å).<sup>[42]</sup> The hydrogen ions in amine group create coordinated bonds with  $I^-$  ion in perovskite lattice. In this study, the perovskite films were fabricated using a hot casting method in air (Experimental Section). The photovoltaic performances of various compositions ( $Aa^+$  ions incorporated into  $MAPbI_3$ ) were first investigated to reveal the effect of ion incorporation on the PCE of fabricated devices. As shown in **Figure 1b**, the PCE of both devices decreases as the incorporated concentration is higher than 5.0 mol%. It is believed that  $Aa^+$  ions are relatively bulky and it is troublesome to form a 3D perovskite structure with lead iodide ( $PbI_2$ ). Therefore, an excess of  $Aa^+$  ions would be vulnerable to PCE of perovskite devices. As a result, the ratio of  $Aa/MA$  is fixed at 5 mol% to further explore the stoichiometric effect of ammonium salts to  $PbI_2$ . The valance band and conduction band of OHPVSK mainly consist of iodide p orbital and uncoordinated lead p orbital. Therefore, the stoichiometry of ammonium salts and lead halide in crystalized perovskite films plays a primary role in manipulating the intrinsic semiconductor

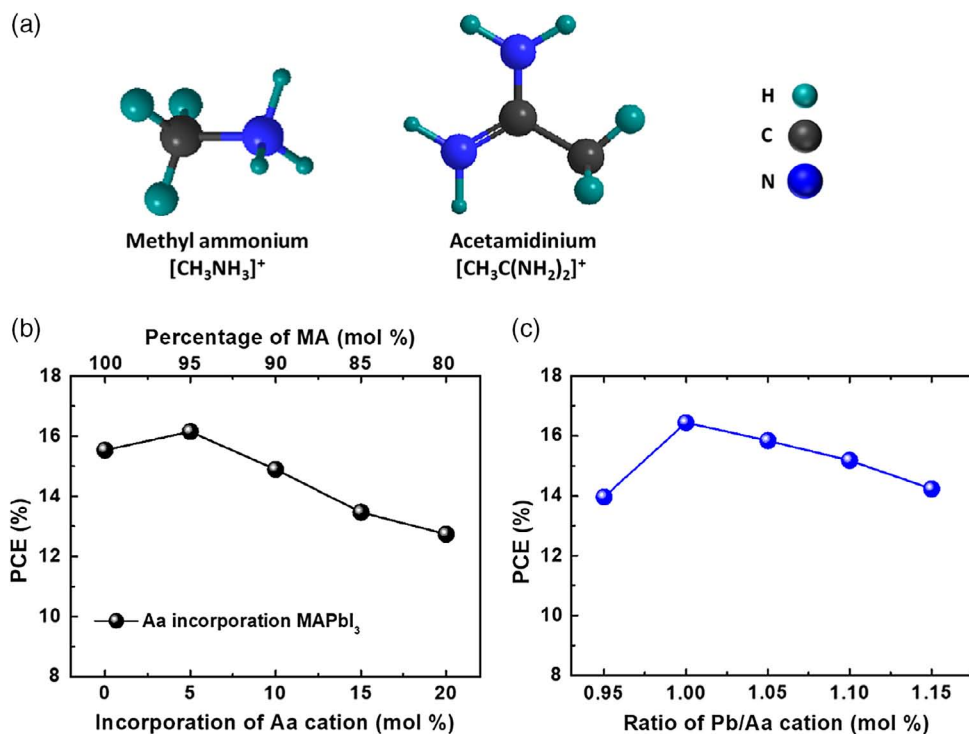


**Figure 1.** Chemical structures of a) A-site cations. Effect of Aa-incorporated MAPbI<sub>3</sub> on the PCE of devices: b) A-site cation ratio and c) B-site/A-site cation ratio.

properties of perovskite films.<sup>[43,44]</sup> As shown in Figure 1c, applying an equivalent stoichiometry of B-site/A-site cation can attain the highest PCE for both cases (5 mol% Aa-incorporated MAPbI<sub>3</sub>). Therefore, a 5 mol% Aa-incorporated MAPbI<sub>3</sub> (Aa-MAPbI<sub>3</sub>) with an equal B-site/A-site cation ratio is applied for further investigation.

To characterize the crystal structure of perovskite films after incorporating Aa<sup>+</sup> ion, XRD were conducted to observe the lattice evolution of perovskite thin films. As shown in Figure S1, Supporting Information, all perovskite thin films have high crystallinity without any impurity PbI<sub>2</sub> phases at the angle of 12.5°. It indicates that the precursors (MAI, AaI, and PbI<sub>2</sub>) are completely transformed to crystallized perovskite thin films. Using a small amount of Aa<sup>+</sup> cation incorporation in MAPbI<sub>3</sub> perovskite film, the ionic radius difference between two cations (Aa<sup>+</sup> and MA<sup>+</sup> ion) is relatively close to each other. That makes them difficult to observe an obvious peak shift in their XRD patterns (Figure S1a, Supporting Information). The expansion of XRD pattern (Figure S1b, Supporting Information) from 19.5° to 20.5° shows a slight peak shift of 0.05° for Aa-MAPbI<sub>3</sub> film compared with MAPbI<sub>3</sub> film. The peak shifting forward a small angle indicates that the lattice of perovskite structure expands after Aa<sup>+</sup> cation incorporated into MAPbI<sub>3</sub>. In addition, the electron density around the nitrogen of Aa<sup>+</sup> ions is expected to be different from that of MA<sup>+</sup> ion. It can be distinguished using an X-ray photoelectron spectroscopy (XPS) analysis by tracing the binding energies of nitrogen 1s orbital of Aa<sup>+</sup> ions in Aa-MAPbI<sub>3</sub>. The XPS spectra of MAPbI<sub>3</sub> and Aa-MAPbI<sub>3</sub> perovskite films are shown in Figure S2, Supporting Information.

In Figure S2a, Supporting Information, the MAPbI<sub>3</sub> film has only one peak (401.3 eV) representing nitrogen 1s orbital from MA<sup>+</sup> ions (C–NH<sub>2</sub>). However, the Aa-MAPbI<sub>3</sub> generates another peak at 399.3 eV, which is referred to as C=NH<sub>2</sub><sup>+</sup> from Aa<sup>+</sup> ions (Figure S2b, Supporting Information). Moreover, the PL mapping and surface potential mapping were adopted to examine the potential phase segregation of Aa-MAPbI<sub>3</sub> films. In Figure S3, Supporting Information, the PL peak position of both MAPbI<sub>3</sub> and Aa-MAPbI<sub>3</sub> films is located at 765 ± 2 nm. No obvious shift of PL emission in Aa-MAPbI<sub>3</sub> film indicates there is negligible phase segregation. By comparison of topography (Figure S4a,b, Supporting Information) and surface potential mapping (Figure S4c,d, Supporting Information), the differences of surface potential appear at the grain boundaries rather than at crystals of perovskite films under UV–A illumination. The results confirm the Aa<sup>+</sup> ions are incorporated into the MAPbI<sub>3</sub> perovskite films with negligible phase segregation.

For the long-term stability aspect of OHPSCs, humidity and thermal stresses are commonly considered as two critical factors affecting the stability of perovskite active layer. Although the current encapsulation techniques are good enough to adequately seal most of the electronic devices, the high environmental tolerance properties of perovskite films are still in need of consideration to prolong the lifetime of OHPSCs. To explore the intrinsic stability of OHPSCs, we first tested the perovskite devices without an encapsulation under various stresses of humidity and heat. In the case of humidity stress tests, all perovskite devices were placed in ambient of Taiwan summer day (30–38 °C and

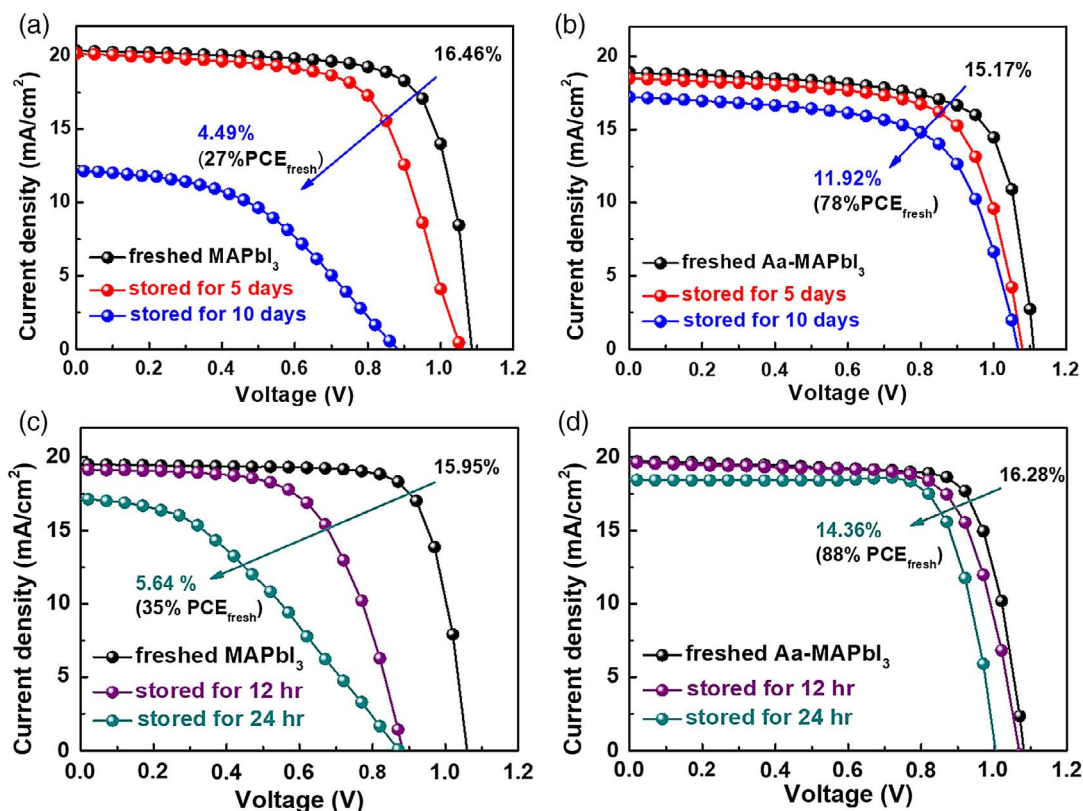
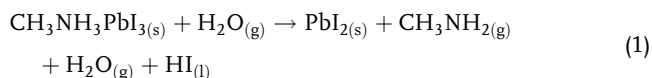


**Figure 2.** Performance of perovskite devices after subjecting to environmental stresses: a) MAPbI<sub>3</sub>, and b) Aa-MAPbI<sub>3</sub> under humidity stress (30–38 °C and 60–80% RH in air); c) MAPbI<sub>3</sub> and d) Aa-MAPbI<sub>3</sub> under thermal stress (85 °C in dry N<sub>2</sub>).

60–80% RH). The performances of OHPSCs under humidity stress are shown in **Figure 2a,b**. Although no apparent changes in devices were observed with naked eyes, the PCE of the device with MAPbI<sub>3</sub> dropped after a 5-day aging as shown in **Figure 2a**. The reduction in PCE is mainly attributed to the  $V_{oc}$  drop in the device. After a 10-day aging, the PCE of MAPbI<sub>3</sub> dramatically decreased to 4.49% corresponding to only 27% initial PCE remained ( $PCE_{fresh}$ ). However, the PCE of device with Aa-MAPbI<sub>3</sub> film could respectively maintain 78% of its  $PCE_{fresh}$  (**Figure 2b**). The large drop in the PCE of the MAPbI<sub>3</sub> device is due to the reaction between moisture and perovskite film and the generation of methylamine according to the following reaction<sup>[45,46]</sup>



We expect that large amounts of H–I coordinated bonds are produced by inducing the Aa<sup>+</sup> ions in perovskite lattice. The stabilized ions exhibit a higher activation energy in the reaction. Moreover, the high boiling points of acetamidine (CH<sub>3</sub>(CH=NH)NH<sub>2</sub>) molecules will hinder the reaction to occur as well. In contrast, the thermal stability tests of devices were carried out at 85 °C in dry N<sub>2</sub>. The results and their performances are shown in **Figure 2c,d**. The devices with Aa-MAPbI<sub>3</sub> film exhibits higher PCEs than the MAPbI<sub>3</sub> device after one day at

85 °C (88% vs 35%  $PCE_{fresh}$ ). Thus, the stability of perovskite devices with Aa<sup>+</sup> ion incorporated MAPbI<sub>3</sub> films can be greatly enhanced as subjected to humidity or thermal stress.

To gain insights into environmental tolerance of MAPbI<sub>3</sub> and Aa-MAPbI<sub>3</sub> films, the change in crystal structure and chemical composition of the films were systematically investigated using various analytical instruments. **Figure 3** shows the crystal structure evolution of perovskite films under humidity stress using XRD. The fresh film exhibits strong characteristic peaks at the angles of 14.02° and 20.04° that are referred to as the (110) and (112) planes of OHPVSK. **Figure 3a** shows that an impurity phase of PbI<sub>2</sub> (12.74°) in MAPbI<sub>3</sub> films could be detected after 5 day aging in humidity (30–38 °C and 60–80% RH in air). In contrast, in the Aa-MAPbI<sub>3</sub> film, a pure perovskite crystal structure unchanged after 10-day aging in humidity (**Figure 3b**). It revealed that incorporation of Aa<sup>+</sup> ions into MAPbI<sub>3</sub> films indeed stabilize the perovskite crystal structure.

The changes in XRD patterns of perovskite films under the thermal stress (85 °C in dry N<sub>2</sub>) are also shown in **Figure 3c,d**. The stoichiometric imbalance of ammonium salts induced the PbI<sub>2</sub> phase in MAPbI<sub>3</sub> film after subjecting to thermal stress for 12 h as shown in **Figure 3c**. The crystal structure of the Aa-MAPbI<sub>3</sub> film is stable after a 24 h thermal stress test (**Figure 3d**). However, we still observed a minor reduction in PCE under 24 h thermal stress (**Figure 2d**), why? A more sensitive technique, ToF-SIMS was used to gain the chemical composition changes in the depth profile of the devices.

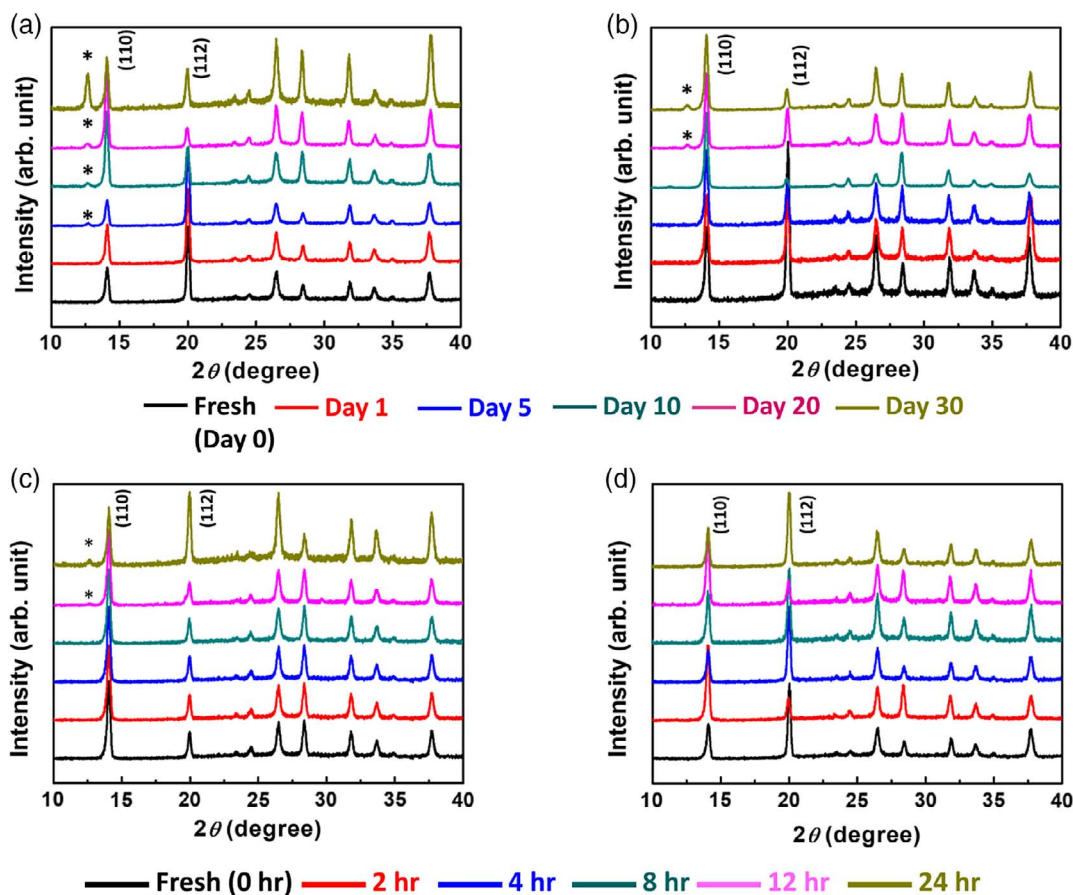


**Figure 3.** XRD patterns of perovskite films: a) MAPbI<sub>3</sub> and b) Aa-MAPbI<sub>3</sub> before and after aging in a humidity condition (30–38 °C and 60–80% RH in air); c) MAPbI<sub>3</sub> and d) Aa-MAPbI<sub>3</sub> under thermal stress (85 °C in dry N<sub>2</sub>). \*symbol refers to the (001) plane of PbI<sub>2</sub>.

The detailed components in perovskite devices and their corresponding fragments of depth profiling in ToF-SIMS depth profiles are shown in Figure S5, Supporting Information. The ToF-SIMS patterns of fresh and 10-day aging devices with the corresponding MAPbI<sub>3</sub> and Aa-MAPbI<sub>3</sub> films are shown in Figure 4. Fresh devices fabricated from either MAPbI<sub>3</sub> or Aa-MAPbI<sub>3</sub> films show similar trends in depth profiles (Figure 4a-1, b-1). The peaks in –Ion mode of I<sup>–</sup> ion at Ag/PC<sub>61</sub>BM interface are attributed to the ionization yield of I<sup>–</sup>. During ToF-SIMS analysis, the secondary ion intensity of species A can be described as Equation (2)

$$i_A^s = I^p Y \alpha_A \eta_A \theta_A X_A \quad (2)$$

where the measured signal intensity  $i_A^s$  depends on the primary ion intensity ( $I^p$ ), material sputter yield ( $Y$ ), ionization probability of species A ( $\alpha_A$ ), transmission efficiency of ionic species A in the ToF-SIMS system ( $\eta_A$ ), isotopic abundance ( $\theta_A$ ), and surface concentration of species A ( $X_A$ ). Under the same analysis condition, it is reasonable to assume that  $I^p$ ,  $\eta_A$ , and  $\theta_A$  are identical among different samples. Given the same  $X_A$  value, however,  $i_A^s$  can still be remarkably different because sputter yield ( $Y$ ) and ionization probability ( $\alpha_A$ ) is highly matrix-dependent. As a result, a sudden change in slope or a peak at the interface can be commonly

seen in a ToF-SIMS depth profile, which can be attributed to matrix effect. Because of matrix effect, the I<sup>–</sup> intensity near the Ag/PC<sub>61</sub>BM interface was enhanced because iodine could easily withdraw electrons from Ag, which significantly increased the ionization probability. A sharp peak from Ag<sup>+</sup> in +Ion mode at the same interfaces also occurs due to the synthetic phenomena of matrix effect. In Figure 4a-2, b-2, an obvious difference in depth profiles of ToF-SIMS patterns before and after 10-days humidity aging implied that the I<sup>–</sup> ions tend to migrate and accumulate at Ag/PC<sub>61</sub>BM interface. However, due to the matrix effect, the I<sup>–</sup> intensity should not be compared directly. In an aim to quantitatively describe the degree of I<sup>–</sup> migration relatively, the migration factor of I<sup>–</sup> was introduced and calculated by the following Equation (3). Focusing on the device with MAPbI<sub>3</sub>, the iodide peak intensity increases from 0.092 to 0.320 after 10-days humidity stress (Figure 4a-1, a-2). However, the peak intensity for Aa-MAPbI<sub>3</sub> device increases from 0.122 to 0.238. (Figure 4b-1, b-2) The migration factors of I<sup>–</sup> ion in MAPbI<sub>3</sub> and Aa-MAPbI<sub>3</sub> devices were estimated as 1.81:1.00, relatively after normalization (Figure S6a, Supporting Information). A significant reduction in I<sup>–</sup> migration factor in Aa-MAPbI<sub>3</sub> device reveals that the increased numbers of H–I bonds from Aa<sup>+</sup> ions incorporation could immobilize I<sup>–</sup> ions as the device under humidity stress. Figure 5 shows the ToF-SIMS depth

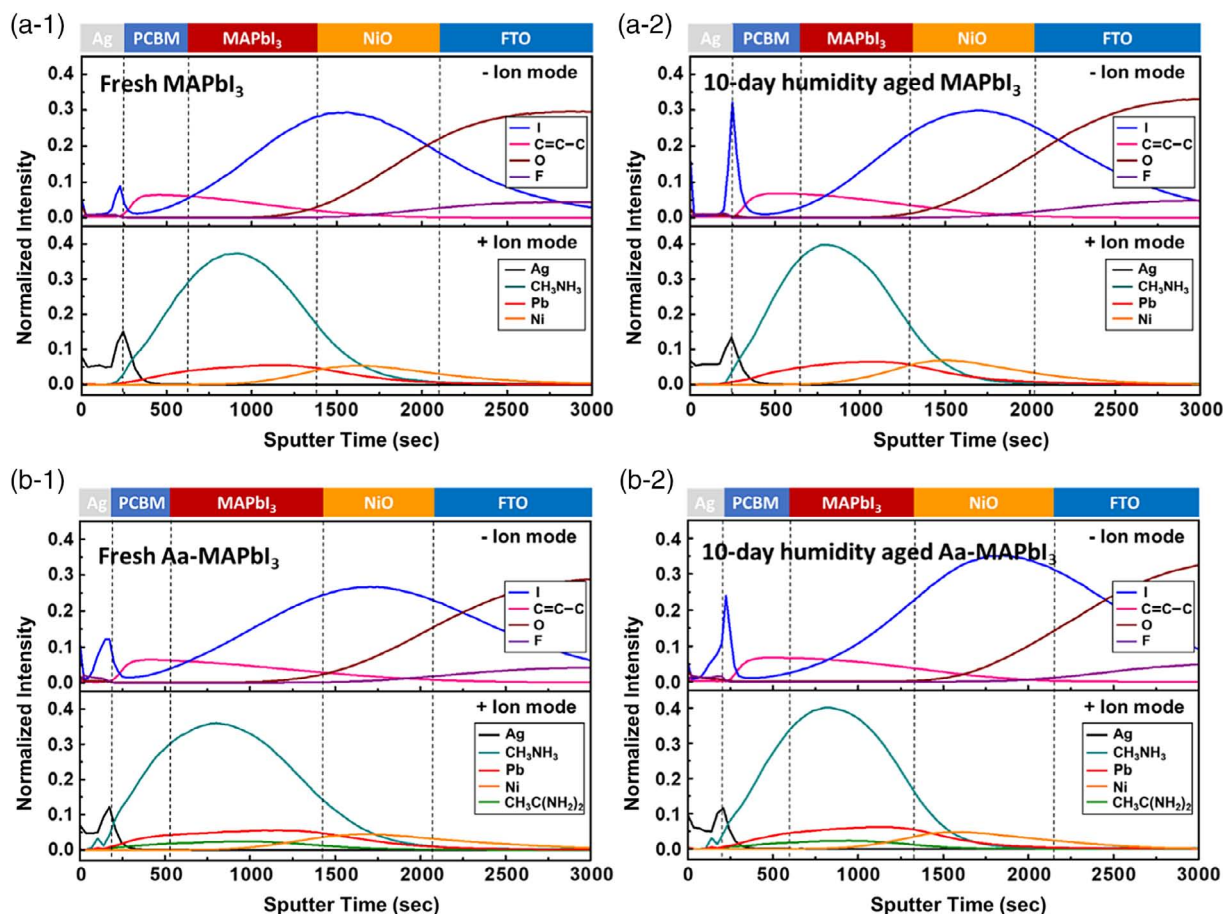


**Figure 4.** ToF-SIMS of perovskite devices: a-1) fresh MAPbI<sub>3</sub> and b-1) fresh Aa-MAPbI<sub>3</sub>; a-2) MAPbI<sub>3</sub> and b-2) Aa-MAPbI<sub>3</sub> after 10-day humidity stress tests in air (30–38 °C and 60–80% RH).

profiles of devices under 24 h thermal stress tests. The same depth profiles of fresh devices with MAPbI<sub>3</sub> and Aa-MAPbI<sub>3</sub> films in Figure 4 and 5 manifested the devices fabricated using hot casting method have a good reproducibility from batch to batch. After devices were subjected to thermal stress, the iodide peak intensity increases from 0.125 to 0.223 for MAPbI<sub>3</sub> device. However, the peak intensity for Aa-MAPbI<sub>3</sub> device increases from 0.183 to 0.226. The migration factors of I<sup>-</sup> ion in MAPbI<sub>3</sub> and Aa-MAPbI<sub>3</sub> devices after 24 h thermal aging were calculated as 1.44:1.00, relatively after normalization (see in Figure S4b, Supporting Information). As shown in Figure 5a-2, the I<sup>-</sup> ions in MAPbI<sub>3</sub> device tend to migrate from perovskite film to electron-deficient Ag electrode with the assistance of thermal stress. However, the I<sup>-</sup> ion peak shift in Aa-MAPbI<sub>3</sub> device is hindered. (Figure 5b-2). The results indicate that incorporated Aa plays an effective role in preventing I<sup>-</sup> ion migration in MAPbI<sub>3</sub> perovskite films under thermal aging as well.

$$\text{Migration factor} = (\text{peak value of I}^-)_{\text{aged}} / (\text{peak value of I}^-)_{\text{fresh}} \quad (3)$$

The study of ToF-SIMS clearly indicates the I<sup>-</sup> ion migration present in the devices. Subsequently, such mobile I<sup>-</sup> ions in

OHPSC would create electron trap states in perovskite films. To explore the changes in electron trap density of perovskite films, the *I*-*V* curves of electron-only devices fitting with SCLC model were performed and shown in Figure S7, Supporting Information. The trap fill voltage (*V*<sub>TFL</sub>) located at the transient point of ohmic region and SCLC region is used to determine the trap density using the following Equation (4)

$$V_{\text{TFL}} = \frac{eN_t d^2}{2\epsilon\epsilon_0} \quad (4)$$

where *e* is the elementary charge, *ε* and *ε*<sub>0</sub> are respectively the dielectric constant and the permittivity of free space in vacuum of MAPbI<sub>3</sub> perovskite, *N*<sub>*t*</sub> is the trapped density of the film, and *d* is the thickness of perovskite films (cross-sectional scanning electron microscopy [SEM] images in Figure S8c,d, Supporting Information). The results are summarized in Table 1. Initially, the electron trap densities of fresh MAPbI<sub>3</sub> and Aa-MAPbI<sub>3</sub> films are calculated as 7.67 × 10<sup>15</sup> and 5.86 × 10<sup>15</sup> (number cm<sup>-3</sup>), respectively. The less trap density of Aa-MAPbI<sub>3</sub> film indicates the film has better quality than MAPbI<sub>3</sub> film. Then, the films were subjected to either humidity or thermal stress. Afterward, the PC<sub>61</sub>BM film was deposited on

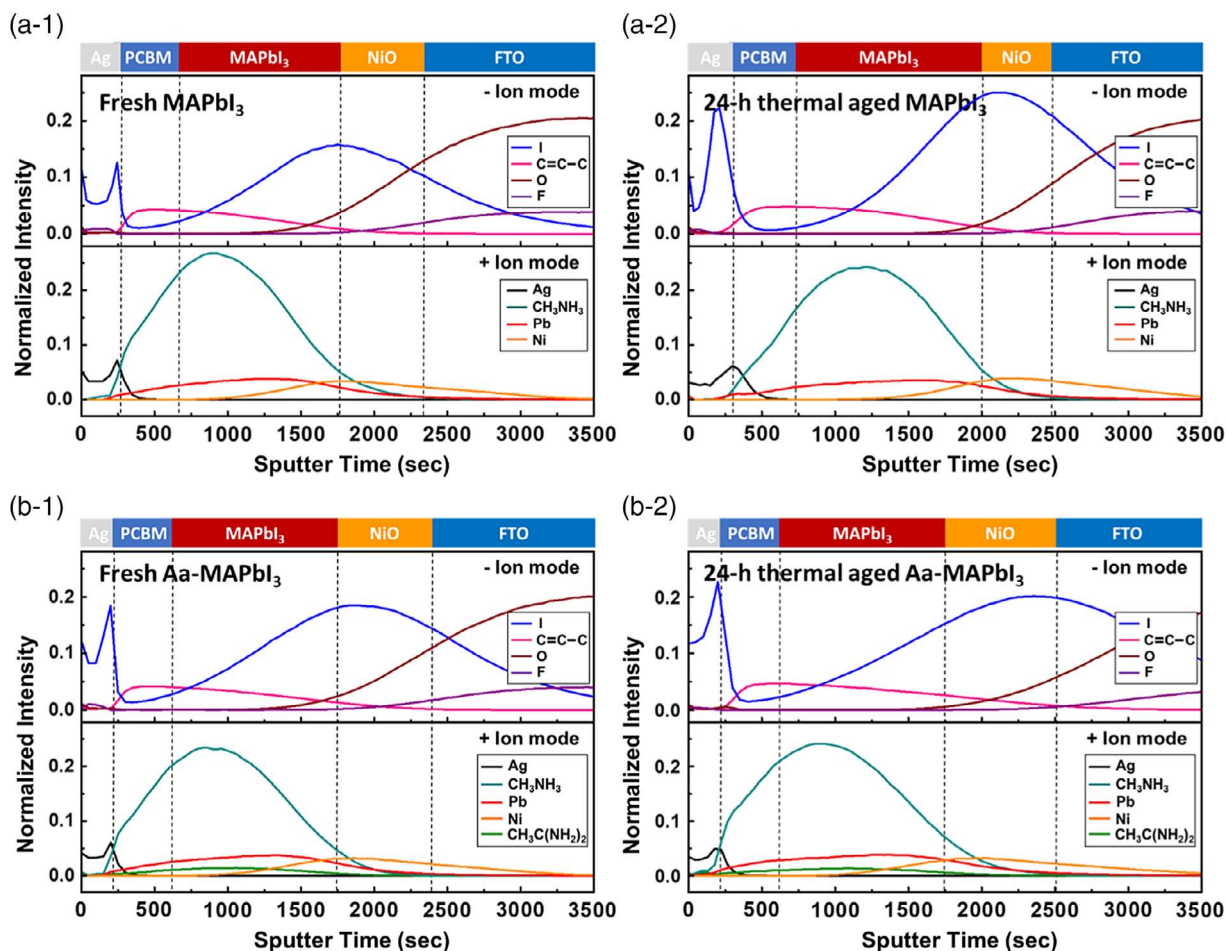


**Figure 5.** ToF-SIMS of perovskite devices. a-1) fresh MAPbI<sub>3</sub> and b-1) fresh Aa-MAPbI<sub>3</sub>; a-2) MAPbI<sub>3</sub> and b-2) Aa-MAPbI<sub>3</sub> after 24 h thermal stress tests in dry N<sub>2</sub>.

**Table 1.** Electron trap densities of MAPbI<sub>3</sub> and Aa-MAPbI<sub>3</sub> films.

Perovskite material	Testing condition	V <sub>TFL</sub> [V]	Trap density [number ((cm) <sup>-3</sup> )]
MAPbI <sub>3</sub>	Fresh	0.78	7.67 × 10 <sup>15</sup>
	Humidity stress	1.76	1.73 × 10 <sup>16</sup>
	Thermal stress	1.13	1.11 × 10 <sup>16</sup>
Aa-MAPbI <sub>3</sub>	Fresh	0.70	5.86 × 10 <sup>15</sup>
	Humidity stress	0.89	7.45 × 10 <sup>15</sup>
	Thermal stress	0.86	7.24 × 10 <sup>15</sup>

the aged perovskite film to avoid aging effect of PC<sub>61</sub>BM film. The electron trap density of MAPbI<sub>3</sub> films was increased from 7.67 × 10<sup>15</sup> to 1.73 × 10<sup>16</sup> (number cm<sup>-3</sup>) under humidity stress and to 1.11 × 10<sup>16</sup> (number cm<sup>-3</sup>) under thermal stress. In contrast, the perovskite films incorporated with Aa<sup>+</sup> ions only had a slight increase in electron trap density after either humidity or thermal stress.

The steady-state PL spectrum and TR-PL spectrum of perovskite films without a quenching layer are shown in Figure S9a,b,

Supporting Information. The strongest PL intensity and longest carrier lifetime of Aa-MAPbI<sub>3</sub> film indicates the carriers in it exhibit the least nonradiative recombination compared with the others. Surprisingly, incorporating Aa<sup>+</sup> ion into MAPbI<sub>3</sub> perovskite film does not only improve the stability of the device but also enhance the photovoltaic performance. To alleviate the drawbacks of existing defects in perovskite films, a technique of dipolar ion passivation following the previous study<sup>[30]</sup> was also applied to optimize the PCE of OHPSC. The depth profiles of ToF-SIMS shown in Figure S10a,b, Supporting Information clarify that the dipolar ions (S-C-H fragment) entirely diffused into perovskite films through grain boundaries. It helps dipolar ion and possibly passivated the defects in perovskite films. The distribution of photovoltaic performance of 24 devices are shown in Figure 6a–d. Taking the advantage of the minor nonrecombination properties of carriers in Aa-MAPbI<sub>3</sub> films, they can be utilized in an efficient pathway for reducing the energy loss of such devices. Therefore, the V<sub>oc</sub> of Aa-MAPbI<sub>3</sub> device can be boosted around 50 mV to 1.13 V (averaged) compared with 1.08 V of MAPbI<sub>3</sub> devices (Figure 6a). The relatively low rate of nonradiative recombination does not only reduce V<sub>oc</sub> loss of devices but also prolong the carrier diffusion length. Figure S11a,b,

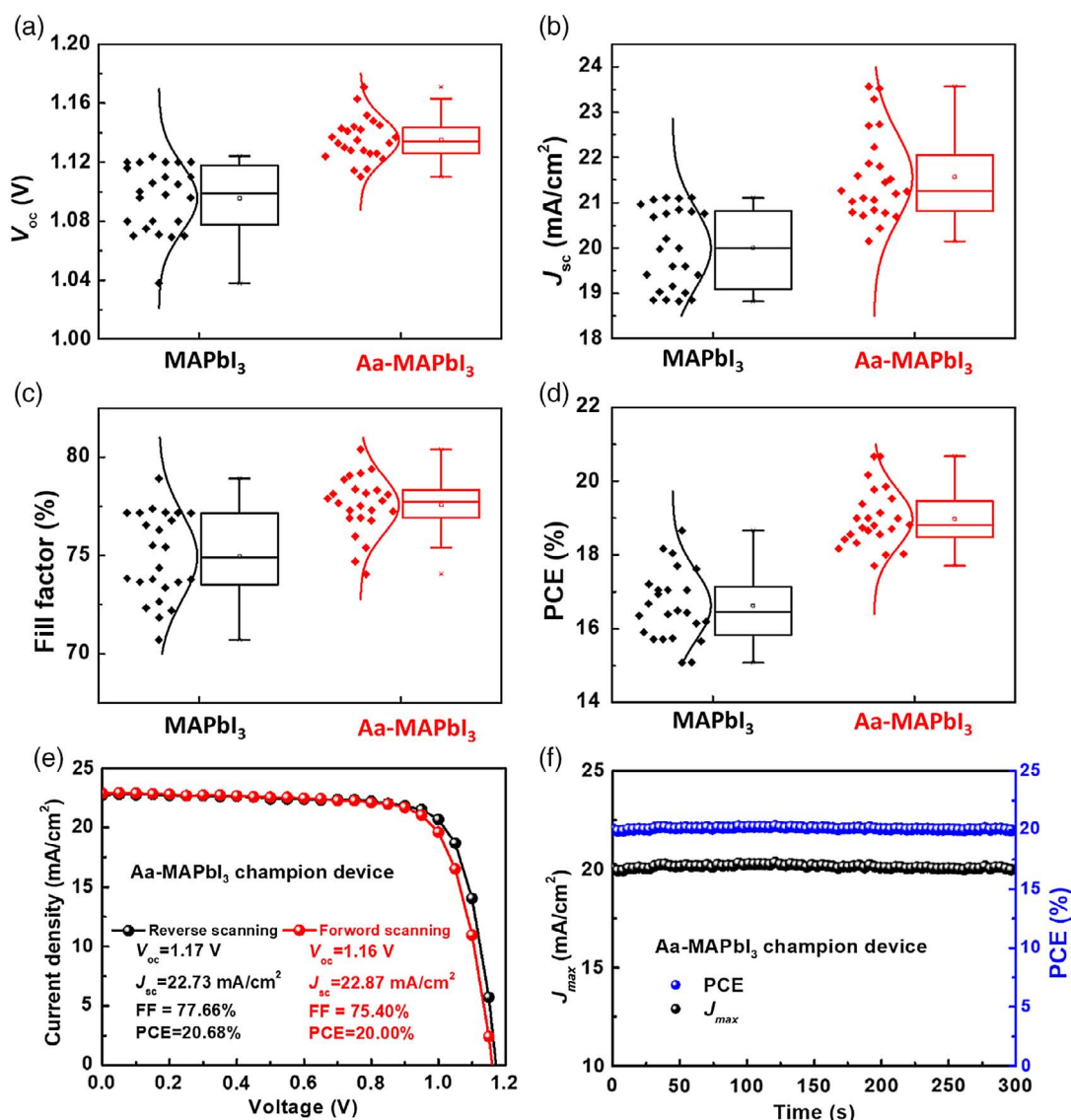


**Figure 6.** Distribution of photovoltaic performances of 24 perovskite devices: a)  $V_{oc}$ , b)  $J_{sc}$ , c) fill factor, and d) PCE; Performance of a championed Aa-MAPbI<sub>3</sub> device: e)  $J-V$  curves, f) steady-state photocurrent output and PCE measured at the maximum power point (applied bias = 1.00 V).

Supporting Information, show the TR-PL spectra of MAPbI<sub>3</sub> and Aa-MAPbI<sub>3</sub> films with and without quenching layers. Here, PC<sub>61</sub>BM films were applied on the perovskite films as electron quenching layer, whereas PTAA films were served as the hole quenching layer. The diffusion lengths of perovskite films were calculated using the 1D diffusion approximation equation<sup>[47]</sup> and listed in Table S1, Supporting Information. Both electron and hole diffusion lengths of Aa-MAPbI<sub>3</sub> are longer than that of MAPbI<sub>3</sub> films. The longer diffusion length of Aa-MAPbI<sub>3</sub> films directly represents the higher current density as shown in Figure 6b. The high film quality of Aa-MAPbI<sub>3</sub> films with low defect densities helps to obtain a high fill factor (Figure 6c). As a result, the averaged PCE of 5 mol% Aa<sup>+</sup> ion-incorporated MAPbI<sub>3</sub> devices was greatly enhanced from 16.62% to 18.98% (Figure 6d). The PCE of champion device was achieved at 20.68% without hysteresis as shown in

Figure 6e. Its steady-state photocurrent output in Figure 6f also represents a stable power output during continuous operation in air. The continuous PL spectra in Figure S12, Supporting Information, again validate that the Aa-MAPbI<sub>3</sub> perovskite film exhibited a relatively stable PL intensity for over a 15 min continuous measurement. The results reconfirm that a minor effect of nonradiative recombination occurs in Aa-MAPbI<sub>3</sub> film compared with the others.

Due to the intrinsic properties improvement of Aa-MAPbI<sub>3</sub>, the devices with encapsulation have an improved stability during damp heat tests (85 °C and 85% RH). **Figure 7** shows average PCE curves summarized from five individual devices with standard deviation bars. The Aa-MAPbI<sub>3</sub> devices could maintain over 80% of PCE<sub>fresh</sub> after 1300 h of damp heat test. It is believed that the ion migration in perovskite films causes adventitious PCE of OHPSC during the light soaking test. With the assistance of large

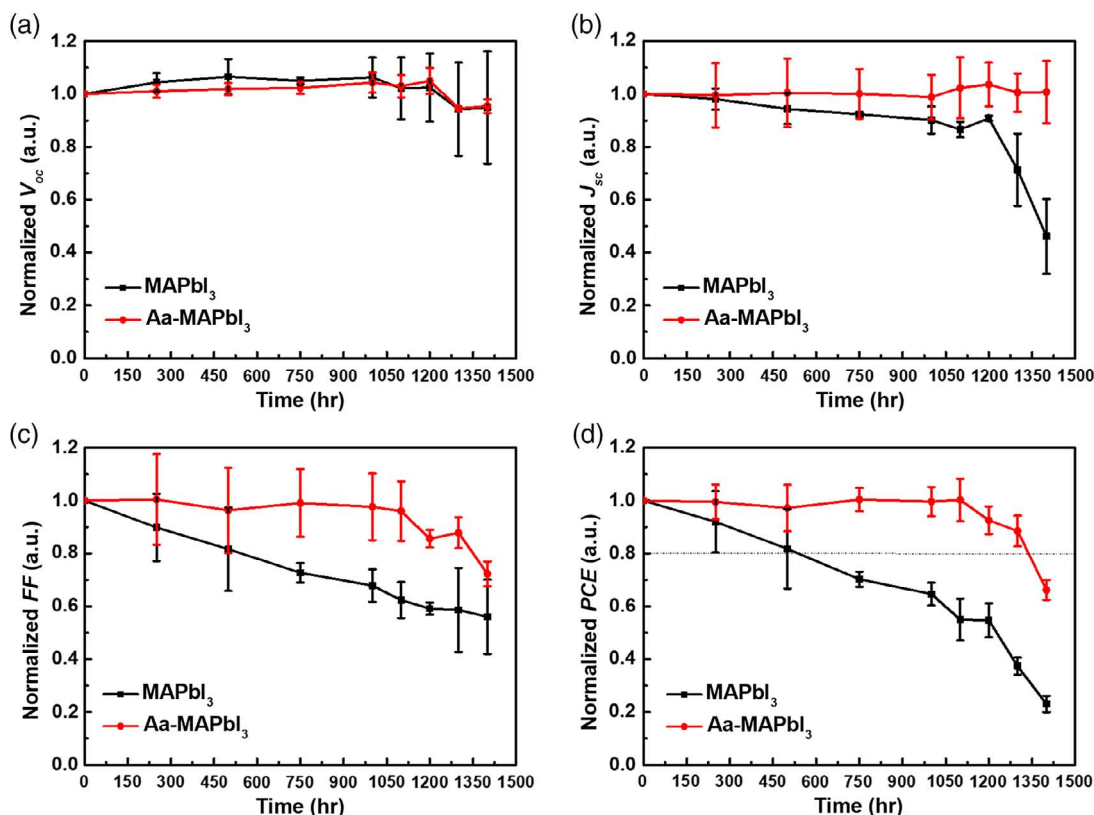


**Figure 7.** Change in performance of perovskite devices during damp heat test (85 °C and 85% RH): a)  $V_{oc}$ , b)  $J_{sc}$ , c) fill factor, and d) PCE.

amount of H–I coordinated bonds from  $Aa^+$  ions, the PCE of such devices can be stabilized during the light soaking test as shown in Figure S13, Supporting Information. It is obvious that the PCE of  $MAPbI_3$  device dropped to 80% of its  $PCE_{fresh}$  after 360 h of the test. In contrast, the device with  $Aa-MAPbI_3$  film could pass over 500 h of the light soaking test.

### 3. Conclusion

This study illustrates a novel candidate,  $Aa^+$  ion, which serves as an A-site cation in the crystal structure of OHPVSK. The effects of  $Aa^+$  ion incorporation into  $MAPbI_3$  perovskite films were systematically examined on its crystal structure, chemical composition, electrical and optical properties, performance, and stability of devices. The results indicated that the  $Aa^+$  cation with a larger amount of coordinated bonds and a higher boiling point compared with  $MA^+$  cation can stabilize the perovskite crystal structure. The  $Aa^+$  ion does not only immobilize  $I^-$  ion under environmental stresses but also reduces the defect density in perovskite films. ToF-SIMS, PL spectroscopy, electronic, and device characterizations were performed to investigate the intrinsic properties of  $Aa-MAPbI_3$  perovskite films. The improvement in crystal quality of  $Aa-MAPbI_3$  perovskite films plays a primary role in enhancing the long-term stability of such devices during damp heat and light soaking tests. In addition, the PCE of such a planar p-i-n  $Aa-MAPbI_3$  device was enhanced from 18.60% to 20.68% compared with the  $MAPbI_3$  device. This novel strategy

of such facile cation incorporation is successfully applied in air, and is considered as a promising method to fabricate high-quality stable perovskite solar cells using conventional upscale coating technology. This study is hoped to shed lights on the mass production and further commercialization of such OHPSCs.

### 4. Experimental Section

**Material and Method:** In this study, the chemicals including methylammonium iodide (99%, STAREK), acetamidinium iodide (99%, STAREK), lead iodide (99.9985%, Alfa Aesar), 6,6-phenyl- $C_{61}$ -butyric acid methyl ester ( $PC_{61}BM$ , 99%, STAREK), polyethyemine (branched PEI, 80%, Sigma-Aldrich), poly[bis(4-phenyl)(2,4,6-trimethylphenyl)amine] ( $M_n = 7,000-10,000$ , Sigma-Aldrich), poly(methyl methacrylate) ( $M.W. = 35,000$ , Acros Organics), lithium fluoride (99.99%, Sigma-Aldrich), nickel acetate tetrahydrate (98%, Kanto Chemicals), gamma butyrolactone (99%, Acros Organics), dimethyl sulfoxide (99.7%, Acros Organics), anhydrous ethanol (99.5%, Sigma-Aldrich), isopropanol (99.5%, Acros Organics), toluene (99.5%, Acros Organics), and chlorobenzene (99%, Acros Organics) were used without any pretreatments or purifications.

For dipolar ion passivation, TEACI was synthesized as described in the previous study.<sup>[30]</sup> Briefly, 17.30 g of 2-(aminomethyl)thiophene (98%, Tokyo Chemical Industry Co., Ltd.) was first transferred into a three-necked bottle and then 4.14 g of hydrochloric acid (36.5–38.0%, Sigma-Aldrich) was dropped into the solution with a stir. After vigorous stirring for 2 h in an ice bath, the appearance of the mixture became a mild yellow solution. The solvent was removed by using a rotary evaporator and the mild yellow color and dish-like reactant was then collected

in a 50 mL vial bottle. The reactant was further washed with diethyl ether (99%, Fisher) until its color faded from mild yellow to white. Subsequently, the reactant was purified using a recrystallization method. Finally, the white reactant was dried in a vacuum oven for 12 h and stored in an inert atmosphere.

**Device Fabrication:** The protocol of a p-i-n hot casting perovskite device followed by the previous study.<sup>[30,48]</sup> Fluorine-doped tin oxide (FTO)-coated glass substrates (8 Ω/sq, STAREK) were washed by a particular sequence of dilute cleaner, base solution, methanol, and isopropanol in an ultrasonic bath for 30 min. Subsequently, UV-ozone treatment was conducted to remove organic contaminations and to modify the FTO layer to be a hydrophilic surface. Note that the hydrophilic surface of the substrate plays an important role in a further coating of nickel oxide (NiO) to obtain a uniform hole transport layer. The roughness of NiO is very critical for the sequent deposition because it would affect the following deposited layers and cause detrimental interfacial contact between layers. An equal stoichiometric mole of iodide salts (MAI and AaI) and PbI<sub>2</sub> in the cosolvent system dimethyl sulfoxide and gamma-butyrolactone in a 3:7 volume ratio with 0.6 M was applied to produce precursors (MAPbI<sub>3</sub> and AaPbI<sub>3</sub>). To obtain Aa-MAPbI<sub>3</sub> precursors, the as-prepared solutions (AaPbI<sub>3</sub>) were respectively mixed with a MAPbI<sub>3</sub> solution by a desired ratio (0–20 mol%) before coating. Prior to perovskite film deposition, the as-prepared substrates (FTO/NiO) and as-prepared precursor solution were preheated at 150 and 70 °C on a hot plate, respectively, for 10 min to reach thermal equilibrium. Taking MAPbI<sub>3</sub> for an example, 55 μL of perovskite precursor solution was quickly dripped onto the hot substrate and spin-coated at 4000 rpm for 15 s as soon as possible. At the beginning of spin-coating process, the transparent perovskite precursor changed to a black solid film. It indicated the precursor turned to a crystallized perovskite film.

To improve PCE of devices, the passivation procedure was conducted using TEACl and the protocol of passivation was following the previous study.<sup>[30]</sup> Subsequently, the electron transport layer (ETL) of 20 mg PC<sub>61</sub>BM dispersed in 1 mL of chlorobenzene was spin-coated onto the passivated perovskite film at 1000 rpm for 30 s. However, in the devices without passivation, the ETL was directly deposited onto the crystallized perovskite film. Prior to capping a silver (Ag) electrode, a work function modifier with 0.1 wt% of polyethylenimine (PEI) dissolved in isopropanol was spin-coated onto the ETL at 4000 rpm for 30 s. Subsequently, 100 nm Ag electrodes were deposited using thermal evaporation with an active area of 0.09 cm<sup>2</sup>. Finally, a 50 nm of LiF antireflective layers were deposited at the front side of the devices (glass side) to reduce the reflection of incident light. To evaluate the device performances, the results were all summarized from 24 devices from four different batches. Each batch consisted of six devices and therefore each composition had 24 individual cells to measure. In addition, the electron-only devices constructed as FTO/compact TiO<sub>2</sub>/perovskite/PC<sub>61</sub>BM/PEI/Au for SCLC model fitting were fabricated to quantify electron trap density in perovskite films. For investigating the diffusion length of perovskite films, TR-PL was used to analyze carrier lifetime of samples. The perovskite films were directly deposited onto glass substrates based on the aforementioned protocol. Solutions of 10 wt% of PMMA in toluene, 10 wt% of PC<sub>61</sub>BM in chlorobenzene, and 10 wt% of PTAA in toluene were deposited on the perovskite films to act as none, electron, and hole quench layers for further examination, respectively.

For aging tests of damp-heat test (85 °C and 85% RH) and light soaking test, five samples were used for each test and results are summarized. FTO substrates of 2.5 cm × 2.0 cm were patterned with crossbar for device fabrication. The devices were fabricated using the same protocol of each layer as mentioned earlier. The electrode then deposited on top of the work function modified layer with a 0.12 cm<sup>2</sup> active area. To entirely seal the devices, a UV curable epoxy resin was utilized. Another 0.8 cm × 1.0 cm glass was capped onto the device. A UV-A lamp (wavelength = 365 nm) with 1.5 W was used to cure the epoxy resin. Finally, a butyl rubber paste was attached by a thermal-pressing method at the edge of the top sealing glass to retard edge leakage. For damp heat tests, the devices were then placed into a humidity (85% RH) and temperature (85 °C) controllable oven (Terchy, HRMB-80) for testing. However, the light soaking test, a xenon lamp (STAREK) of 100 mW cm<sup>-2</sup>

with an UV filter was applied for light soaking test. The encapsulated devices were all tested in air with a force convection flow to keep the operating temperature at 40–50 °C.

**Characterization of Material and Devices:** The solar simulator source (YAMASHITA DENSO, YSS-200 A, class AAA) equipped with a 1600 W xenon short-arc lamp was used to analyze the photovoltaic performance of devices. The photocurrent density (*I*)-voltage (*V*) curve of solar cell devices were all measured in air under A.M. 1.5 irradiation (100 mW cm<sup>-2</sup>) and recorded by the Keithley 2410 SourceMeter. Prior to the measurements, the light intensity of the solar simulator was calibrated using a KG-5 filtered monocrystalline silicon standard cell to adjust miss-matched spectra and to obtain the unity of measurements. The *I*-*V* characteristics of devices were analyzed from both forward -0.2 to 1.2 V and backward (1.2 to -0.2 V) scans. The analysis protocol of ToF-SIMS followed by the previous study.<sup>[49]</sup> Briefly, the gradient of test voltage was fixed at 50 mV or -50 mV with a delay span of 10 ms. All the ToF-SIMS depth profiles were obtained using a PHI TRIFT V nano TOF (ULVAC-PHI, Japan) system with a dual-beam sputter-and-view scheme. During the analysis phase, a pulsed C<sub>60</sub><sup>+</sup> (approximately 8200 Hz, pulse length of 15 ns) rastering over a 50 μm × 50 μm area was used as the primary ion. The kinetic energy of the incident C<sub>60</sub><sup>+</sup> ion was 20 keV and beam current (DC) was set as 0.08 nA. For the sputter phase, a 1 kV Ar<sup>+</sup> beam with a beam current of 400 nA rastering over a 1500 × 1500 μm area was utilized to remove the surfaced materials. For carrier behavior analyses, a 440 nm continuous-wave diode laser (DONGWOO, PDLH-440-25) was applied to excite the perovskite films to quantify steady-state PL, continuous PL, and TR-PL. The TR-PL spectra were recorded by a time-correlated single-photon counting (TCSPC) (WELLS-001 FX, DONGWOO OPTRON) spectrometer at a frequency of 312.5 MHz and delay span of 2 ms. Cross-sectional field-emission scanning electron microscope (FE-SEM) samples were split from an actual device using a mechanical glasscutter and a clip. Images of perovskite films were acquired by an FE-SEM (Hitachi, SU8000, 15 kV voltage, 10.0 mm working distance). The high power (18 kW) X-ray diffractometer (Rigaku TTRAX 3) with Cu Kα radiation (λ = 1.5406 Å) was conducted to characterize the XRD patterns of perovskite films. The trap density and carrier mobility were calculated followed by SCLC model. For quantifying the electron trap density in perovskite films, the architecture of FTO/TiO<sub>2</sub>/perovskites/PC<sub>61</sub>BM/PEI/Au was adopted to measure the *I*-*V* curve of electron-only devices. The trap-filled voltage (*V*<sub>TFL</sub>) can be extracted from the trap-filled condition and the electron trap density in perovskite films were then calculated by the following equation

$$V_{TFL} = \frac{eN_t d^2}{2\epsilon\epsilon_0} \quad (5)$$

where *e* is the primary charge, *N<sub>t</sub>* is the trap density in perovskite film, *d* is the thickness of film, *ε* is the dielectric constant, and *ε<sub>0</sub>* is the permittivity of the perovskite material.

## Supporting Information

Supporting Information is available from the Wiley Online Library or from the author.

## Acknowledgements

This work was financially supported by the “Advanced Research Center For Green Materials Science and Technology” from The Featured Area Research Center Program within the framework of the Higher Education Sprout Project by the Ministry of Education (109L9006) and the Ministry of Science and Technology (MOST 109-2634-F-002-042). The project was also partially supported by the grants from Ministry of Science and Technology (MOST 108-2119-M-002-005, 109-3116-F-002-001-CC2, 106-2923-M-002-004-MY3).

## Conflict of Interest

The authors declare no conflict of interest.

## Keywords

acetamidinium, hot casting, perovskite solar cells, solution processes, stability

Received: April 13, 2020

Revised: May 15, 2020

Published online:

- [1] S. De Wolf, J. Holovsky, S.-J. Moon, P. Löper, B. Niesen, M. Ledinsky, F.-J. Haug, J.-H. Yum, C. Ballif, *J. Phys. Chem. Lett.* **2014**, *5*, 1035.
- [2] Y. Gao, M. Zhang, X. Zhang, G. Lu, *J. Phys. Chem. Lett.* **2019**, *10*, 3820.
- [3] J. Huang, Y. Yuan, Y. Shao, Y. Yan, *Nat. Rev. Mater.* **2017**, *2*, 17042.
- [4] F. Zhang, B. Yang, Y. Li, W. Deng, R. He, *J. Mater. Chem. C* **2017**, *5*, 8431.
- [5] D. P. McMeekin, G. Sadoughi, W. Rehman, G. E. Eperon, M. Saliba, M. T. Hörlantner, A. Haghighirad, N. Sakai, L. Korte, B. Rech, M. B. Johnston, L. M. Herz, H. J. Snaith, *Science* **2016**, *351*, 151.
- [6] M. Abdi-Jalebi, Z. Andaji-Garmaroudi, S. Cacovich, C. Stavrakas, B. Philippe, J. M. Richter, M. Alsari, E. P. Booker, E. M. Hutter, A. J. Pearson, S. Lilliu, T. J. Savenije, H. Rensmo, G. Divitini, C. Ducati, R. H. Friend, S. D. Stranks, *Nature* **2018**, *555*, 497.
- [7] J. Kim, M. I. Saidaminov, H. Tan, Y. Zhao, Y. Kim, J. Choi, J. W. Jo, J. Fan, R. Quintero-Bermudez, Z. Yang, L. N. Quan, M. Wei, O. Voznyy, E. H. Sargent, *Adv. Mater.* **2018**, *30*, 1706275.
- [8] A. Kojima, K. Teshima, Y. Shirai, T. Miyasaka, *J. Am. Chem. Soc.* **2009**, *131*, 6050.
- [9] NREL: Best Research-Cell Efficiencies, <https://www.nrel.gov/pv/assets/pdfs/best-research-cell-efficiencies.20200311.pdf> (accessed: March 2020).
- [10] K. Kwak, E. Lim, N. Ahn, J. Heo, K. Bang, S. K. Kim, M. Choi, *Nanoscale* **2019**, *11*, 11369.
- [11] C. C. Boyd, R. Cheacharoen, T. Leijtens, M. D. McGehee, *Chem. Rev.* **2019**, *119*, 3418.
- [12] N. Aristidou, C. Eames, I. Sanchez-Molina, X. Bu, J. Kosco, M. S. Islam, S. A. Haque, *Nat. Commun.* **2017**, *8*, 15218.
- [13] M. I. Saidaminov, J. Kim, A. Jain, R. Quintero-Bermudez, H. Tan, G. Long, F. Tan, A. Johnston, Y. Zhao, O. Voznyy, E. H. Sargent, *Nat. Energy* **2018**, *3*, 648.
- [14] B. Roose, Q. Wang, A. Abate, *Adv. Energy Mater.* **2019**, *9*, 1803140.
- [15] Z. Wang, Q. Lin, F. P. Chmiel, N. Sakai, L. M. Herz, H. J. Snaith, *Nat. Energy* **2017**, *2*, 17135.
- [16] W.-J. Yin, T. Shi, Y. Yan, *Appl. Phys. Lett.* **2014**, *104*, 063903.
- [17] B. Chen, P. N. Rudd, S. Yang, Y. Yuan, J. Huang, *Chem. Soc. Rev.* **2019**, *48*, 3842.
- [18] S. D. Stranks, *ACS Energy Lett.* **2017**, *2*, 1515.
- [19] G. Nan, X. Zhang, M. Abdi-Jalebi, Z. Andaji-Garmaroudi, S. D. Stranks, G. Lu, D. Beljonne, *Adv. Energy Mater.* **2018**, *8*, 1702754.
- [20] J. Xiang, Y. Li, F. Huang, D. Zhong, *Phys. Chem. Chem. Phys.* **2019**, *21*, 17836.
- [21] C. Ran, J. Xu, W. Gao, C. Huang, S. Dou, *Chem. Soc. Rev.* **2018**, *47*, 4581.
- [22] K. X. Steirer, P. Schulz, G. Teeter, V. Stevanovic, M. Yang, K. Zhu, J. J. Berry, *ACS Energy Lett.* **2016**, *1*, 360.
- [23] W. Tress, N. Marinova, T. Moehl, S. M. Zakeeruddin, M. K. Nazeeruddin, M. Grätzel, *Energ. Environ. Sci.* **2015**, *8*, 995.
- [24] D.-H. Kang, N.-G. Park, *Adv. Mater.* **2019**, *31*, 1805214.
- [25] F. Wang, W. Geng, Y. Zhou, H.-H. Fang, C.-J. Tong, M. A. Loi, L.-M. Liu, N. Zhao, *Adv. Mater.* **2016**, *28*, 9986.
- [26] N. K. Noel, A. Abate, S. D. Stranks, E. S. Parrott, V. M. Burlakov, A. Goriely, H. J. Snaith, *ACS Nano* **2014**, *8*, 9815.
- [27] H. Li, L. Tao, F. Huang, Q. Sun, X. Zhao, J. Han, Y. Shen, M. Wang, *ACS Appl. Mater. Inter.* **2017**, *9*, 38967.
- [28] P. Ru, E. Bi, Y. Zhang, Y. Wang, W. Kong, Y. Sha, W. Tang, P. Zhang, Y. Wu, W. Chen, X. Yang, H. Chen, L. Han, *Adv. Energy Mater.* **2019**, *9*, 1903487.
- [29] W. Chen, Y. Zhou, G. Chen, Y. Wu, B. Tu, F.-Z. Liu, L. Huang, A. M. C. Ng, A. B. Djurišić, Z. He, *Adv. Energy Mater.* **2019**, *9*, 1803872.
- [30] K.-C. Hsiao, M.-H. Jao, B.-T. Li, T.-H. Lin, S. H.-C. Liao, M.-C. Wu, W.-F. Su, *ACS Appl. Energy Mater.* **2019**, *2*, 4821.
- [31] S. Yang, J. Dai, Z. Yu, Y. Shao, Y. Zhou, X. Xiao, X. C. Zeng, J. Huang, *J. Am. Chem. Soc.* **2019**, *141*, 5781.
- [32] Q. Jiang, Y. Zhao, X. Zhang, X. Yang, Y. Chen, Z. Chu, Q. Ye, X. Li, Z. Yin, J. You, *Nat. Photonics* **2019**, *13*, 460.
- [33] M. H. Futscher, J. M. Lee, L. McGovern, L. A. Muscarella, T. Wang, M. I. Haider, A. Fakhruddin, L. Schmidt-Mende, B. Ehrler, *Mater. Horiz.* **2019**, *6*, 1497.
- [34] A. D. Jodlowski, C. Roldán-Carmona, G. Grancini, M. Salado, M. Ralaifarisoa, S. Ahmad, N. Koch, L. Camacho, G. de Miguel, M. K. Nazeeruddin, *Nat. Energy* **2017**, *2*, 972.
- [35] G. Han, H. D. Hadi, A. Bruno, S. A. Kulkarni, T. M. Koh, L. H. Wong, C. Soci, N. Mathews, S. Zhang, S. G. Mhaisalkar, *J. Phys. Chem. C* **2018**, *122*, 13884.
- [36] F. Arabpour Roghabadi, M. Alidaei, S. M. Mousavi, T. Ashjari, A. S. Tehrani, V. Ahmadi, S. M. Sadrameli, *J. Mater. Chem. A* **2019**, *7*, 5898.
- [37] W. Qiu, A. Ray, M. Jaysankar, T. Mercx, J. P. Bastos, D. Cheyns, R. Gehlhaar, J. Poortmans, P. Heremans, *Adv. Funct. Mater.* **2017**, *27*, 1700920.
- [38] D. W. Ferdani, S. R. Pering, D. Ghosh, P. Kubiak, A. B. Walker, S. E. Lewis, A. L. Johnson, P. J. Baker, M. S. Islam, P. J. Cameron, *Energy Environ. Sci.* **2019**, *12*, 2264.
- [39] Y. Fu, M. P. Hautzinger, Z. Luo, F. Wang, D. Pan, M. M. Aristov, I. A. Guzei, A. Pan, X. Zhu, S. Jin, *ACS Cent Sci* **2019**, *5*, 1377.
- [40] P. R. Varadwaj, A. Varadwaj, H. M. Marques, K. Yamashita, *Sci. Rep.* **2019**, *9*, 50.
- [41] C. W. Myung, J. Yun, G. Lee, K. S. Kim, *Adv. Energy Mater.* **2018**, *8*, 1702898.
- [42] W. Travis, E. N. K. Glover, H. Bronstein, D. O. Scanlon, R. G. Palgrave, *Chem. Sci.* **2016**, *7*, 4548.
- [43] M. E.-A. Madjet, A. V. Akimov, F. El-Mellouhi, G. R. Berdiyrov, S. Ashhab, N. Tabet, S. Kais, *Phys. Chem. Chem. Phys.* **2016**, *18*, 5219.
- [44] J. Zhang, M.-h. Shang, P. Wang, X. Huang, J. Xu, Z. Hu, Y. Zhu, L. Han, *ACS Energy Lett.* **2016**, *1*, 535.
- [45] Y. Ouyang, Y. Li, P. Zhu, Q. Li, Y. Gao, J. Tong, L. Shi, Q. Zhou, C. Ling, Q. Chen, Z. Deng, H. Tan, W. Deng, J. Wang, *J. Mater. Chem. A* **2019**, *7*, 2275.
- [46] E. J. Juarez-Perez, L. K. Ono, M. Maeda, Y. Jiang, Z. Hawash, Y. Qi, *J. Mater. Chem. A* **2018**, *6*, 9604.
- [47] A. H. Proppe, R. Quintero-Bermudez, H. Tan, O. Voznyy, S. O. Kelley, E. H. Sargent, *J. Am. Chem. Soc.* **2018**, *140*, 2890.
- [48] H.-C. Liao, P. Guo, C.-P. Hsu, M. Lin, B. Wang, L. Zeng, W. Huang, C. M. M. Soe, W.-F. Su, M. J. Bedzyk, M. R. Wasielewski, A. Facchetti, R. P. H. Chang, M. G. Kanatzidis, T. J. Marks, *Adv. Energy Mater.* **2017**, *7*, 1601660.
- [49] C.-H. Hou, S.-H. Hung, L.-J. Jhang, K.-J. Chou, Y.-K. Hu, P.-T. Chou, W.-F. Su, F.-Y. Tsai, J. Shieh, J.-J. Shyue, *ACS Appl. Mater. Inter.* **2020**, *12*, 22730.